

A hybrid ferromagnetic transmon qubit: circuit design, feasibility and detection protocols for magnetic fluctuations

Halima Giovanna Ahmad,^{1,2,3,*} Valentina Brosco,^{4,5} Alessandro Miano,^{1,†} Luigi Di Palma,¹ Marco Arzeo,² Domenico Montemurro,¹ Procolo Lucignano,¹ Giovanni Piero Pepe,¹ Francesco Tafuri,^{1,6} Rosario Fazio,^{7,1} and Davide Massarotti^{8,3}

¹*Dipartimento di Fisica "Ettore Pancini", Università di Napoli "Federico II", Monte S. Angelo, I-80126 Napoli, Italy*

²*Seeqc, Strada Vicinale Cupa Cinthia, 21, I-80126 Napoli, Italy*

³*CNR-SPIN, UOS Napoli, Monte S. Angelo, via Cinthia, I-80126 Napoli, Italy*

⁴*Institute for Complex Systems, National Research Council and Dipartimento di Fisica, Università "La Sapienza", P.le A. Moro 2, 00185 Rome, Italy*

⁵*Research Center Enrico Fermi, Via Panisperna 89a, 00184 Rome, Italy*

⁶*CNR - Istituto Nazionale di Ottica (CNR-INO), Largo Enrico Fermi 6, 50125 Florence, Italy*

⁷*Abdus Salam ICTP, Strada Costiera 11, I-34151 Trieste, Italy*

⁸*Dipartimento di Ingegneria Elettrica e delle Tecnologie dell'Informazione, Università degli Studi di Napoli Federico II, via Claudio, I-80125 Napoli, Italy*

We propose to exploit currently available tunnel ferromagnetic Josephson junctions to realize a hybrid superconducting qubit. We show that the characteristic hysteretic behavior of the ferromagnetic barrier provides an alternative and intrinsically digital tuning of the qubit frequency by means of magnetic field pulses. To illustrate functionalities and limitation of the device, we discuss the coupling to a read-out resonator and the effect of magnetic fluctuations. The possibility to use the qubit as a noise detector and its relevance to investigate the subtle interplay of magnetism and superconductivity is envisaged.

I. INTRODUCTION

Superconducting qubits are among the most promising paradigms in quantum computation. A wealth of successful experiments proved how efficiently these devices can be manipulated and read-out by commercial electronics, how flexible is their Hamiltonian, how accurate is the control over their quantum state [1–5]. More importantly, the steady progress of nanofabrication techniques and circuit's design brought a strong enhancement of qubit's coherence time that made possible performing practical quantum algorithms [1–5]. The search for combinations of novel materials [6–9], circuitual designs [4, 5, 10, 11] and new protocols for qubits encoding [12, 13] is a very active field of research. The key role of the Josephson junctions in superconducting qubits has also promoted novel efforts for a better understanding their microwave properties, their electrodynamic parameters, and thus their non-linear behavior for the development of alternative approaches for the control and tunability of their functions.

Superconducting quantum circuits have almost exclusively relied on aluminum-aluminum oxide-aluminum (Al/AIO_x/Al) tunnel Superconductor/Insulator/Superconductor (SIS) Josephson junctions (JJs) [4, 11]. However, many exciting phenomena and functionalities can be accessed by exploiting unconventional superconducting systems. This has to be meant

not only as a rush for the best qubit candidate, but also as an advance towards a better understanding and control of a Josephson-based quantum circuit. It is indeed of fundamental importance to explore novel hybrid quantum devices for enhancing both the capabilities of the superconducting electronics [4, 11] and the understanding of the exotic phenomenology that can arise in hybrid unconventional superconducting devices. As an example, in the specific case of tunable transmon qubits [14], which typically use external flux-fields to change the qubit frequency, hybrid superconductor-semiconductor structures [15–23] have been used to enable voltage-tunable transmons (gatemons), in order to provide an alternative tuning of the qubit frequency without introducing flux-noise [17].

In this work, we focus on another special class of unconventional Josephson devices that use ferromagnetic barriers (SFS JJs). The competition between the superconducting and the ferromagnetic order parameters in these systems allows to build JJs with an intrinsic phase-shift of π [24, 25], providing π -components and *quiet* qubits [6, 26]. SFS JJs in superconducting circuits have been mostly used as passive elements [6] and they have not been considered up to now in the realization of quantum circuits, because of their intrinsic high quasiparticle dissipation [24, 27–30]. This dissipation derives from the metallic nature of standard ferromagnetic barriers, which unavoidably compromises the qubit state measurement and its performances [31, 32]. However, advances in coupling both ferromagnetic layers with insulating barriers inside the JJ (SISFS or SIFS JJs) [33–38] and the ability to exploit intrinsic insulating ferromagnetic materials (SI_fS JJs) [39–44] allow to engineer ferromagnetic JJs characterized by high values of the qual-

* halimagiovanna.ahmad@unina.it

† Current affiliation: Department of Applied Physics, Yale University, New Haven, Connecticut 06520, USA

ity factors and low quasiparticles dissipation [43]. Such tunnel-SFS JJs offer additional functionalities not only in superconducting classical circuits, but also in quantum architectures [6, 43].

We here present a proof of concept study of an innovative protocol for qubit frequency tuning relying on state-of-the art tunnel-SFS JJs. Specifically, we focus on a transmon design featuring a SIS JJ and a SFS JJ inside a SQUID loop capacitively coupled to a superconducting read-out resonator [14]. We name this transmon employing ferromagnetic junctions *ferro-transmon*. We discuss the possibility to provide: (i) a digital tuning of the qubit frequency exploiting the hysteretic nature of the F barrier, and (ii) a novel platform for the study of magnetization dynamics and fluctuations occurring in SFS JJs on a quantum-coherent scale. On one hand, the realization of digital read-out and tunability schemes for superconducting qubits may have a strong impact on the scalability of superconducting quantum systems [13]. On the other hand, the possibility to probe magnetic noise fluctuations [29, 43, 45] provides an additional spectroscopic tool for the barrier dynamics and it may be of crucial relevance for the understanding of the unconventional superconducting transport mechanisms that occur at the S/F interface, including spin-triplet transport [27, 44] and inverse proximity effect [30, 46].

The paper is organized as follows. In Sec. II, we discuss the working-principle behind the ferro-transmon, highlighting advantages, disadvantages and open issues. In Sec. III, we discuss the feasibility of the device: we estimate the ferro-transmon parameters, including the qubit frequency, the ferro-transmon tunability and the read-out resonator dispersive shift as a function of the critical current of the SFS JJ. We compare the obtained results with those reported in literature for non-magnetic qubits [4, 16]. In Sec. IV, we present a qualitative analysis of the dissipation mechanisms, focusing in particular on the impact of SFS JJ's magnetization fluctuations. Finally, we discuss a protocol for the study of magnetization noise spectra relying on tunability of the couplings between the ferro-transmon and different noise sources.

II. FERRO-TRANSMON: A DIGITALLY TUNABLE SUPERCONDUCTING QUBIT

We here discuss the main idea of the ferro-transmon circuit: digital tuning of the qubit frequency, based on the residual magnetization of a ferromagnet, can be achieved by integrating a tunnel-SFS JJ in the SQUID loop of a transmon circuit, schematically reported in Fig. 1 (a). The SQUID loop of the transmon is threaded as usual by an external flux Φ_Z , which is directed along the z -axis. Φ_Z sets the standard cosinusoidal modulation of the SQUID Josephson energy [47, 48]. In addition, in the ferro-transmon circuit a local magnetic flux Φ_L is applied along x or y , *i.e.* perpendicularly to the Josephson transport direction.

The local field Φ_L is related to the magnetization loop of the ferromagnet $4\pi M(H_p)$ as [34–37, 49]

$$\Phi_L(H_p) = H_p d_m a + 4\pi M(H_p) d_F a, \quad (1)$$

where d_F is the thickness of the F barrier, a is the lateral dimension of the tunnel-SFS JJ, d_m is the effective magnetic length of the ferromagnetic barrier [35] and H_p is the field applied along x or y [34, 35]. While the pulsed Φ_L does not directly affect the behavior of the SIS junction, the critical current of the SFS JJ as a function of an external magnetic field H_p along x (y) follows a hysteretic Fraunhofer-like behavior, with a shift of the maximum of the $I_c(H)$ curve that depends on the residual magnetization of the F layer [49]. As an example, in Fig. 1 (b) we report the $I_c(H)$ pattern measured at 10 mK on a SI_fS JJ with a 3.5 nm GdN barrier and area of 49 μm^2 , reported here as a reference. The S electrodes are made of NbN. Additional information about this device can be found in Refs. [42–44], while the fabrication procedure is reported in Refs. [40, 41, 50]. A pulsed magnetic field as that represented in Fig. 1 (c) allows to switch the critical current of the SFS JJ between two discrete values, from now on defined as the low-level (LO) and the high-level (HI) states. As a consequence, also the Josephson energy can be digitally tuned.

Formally, the dependence of the Josephson energy on Φ_Z and Φ_L reads as

$$E_J(\Phi_Z, \Phi_L) = E_{J\Sigma}(\Phi_L) \cos(\pi\Phi_Z/\Phi_0) \cdot \sqrt{1 + d^2(\Phi_L) \tan^2(\pi\Phi_Z/\Phi_0)}, \quad (2)$$

where we set $E_{J\Sigma}(\Phi_L) = E_J^{\text{SIS}} + E_J^{\text{SFS}}(\Phi_L)$ and we denote as $d(\Phi_L)$ the asymmetry parameter,

$$d(\Phi_L) = \frac{E_J^{\text{SIS}} - E_J^{\text{SFS}}(\Phi_L)}{E_J^{\text{SIS}} + E_J^{\text{SFS}}(\Phi_L)}. \quad (3)$$

In Fig. 1 (d), we report the Josephson energy E_J as a function of the external flux Φ_Z applied along the axis z of the SQUID and as a function of the same pulsed magnetic field sequence in Fig. 1 (c) applied along x . In the ferro-transmon SQUID, we consider a SI_fS JJ with GdN barrier as that in Fig. 1 (b), and a Josephson energy for the non-magnetic JJ of standard values commonly found in Al/Nb based transmon qubits, *i.e.* of the order of $E_J^{\text{SIS}} = 10$ GHz [51, 52]. As one can observe, the application of the magnetic field along x allows to tune E_J between two discrete values: before the pulse, I_c is in the HI state. At the end of the pulse I_c reaches the LO state. By applying Φ_Z along the z -axis, instead, we observe the typical cosinusoidal modulation of E_J given by the flux-tunability of the SQUID. In the specific case analyzed, $E_J(\Phi_Z, \Phi_L)$ at $\Phi_0/2$ does not vanish. This typically occurs when the asymmetry of the SQUID reaches $d \sim 1$. As a matter of fact, in the mentioned reference example reported in Fig. 1, the JJs in the SQUID have critical currents that differ by a factor 10, since $I_c^{\text{SFS}} \sim 350$ nA

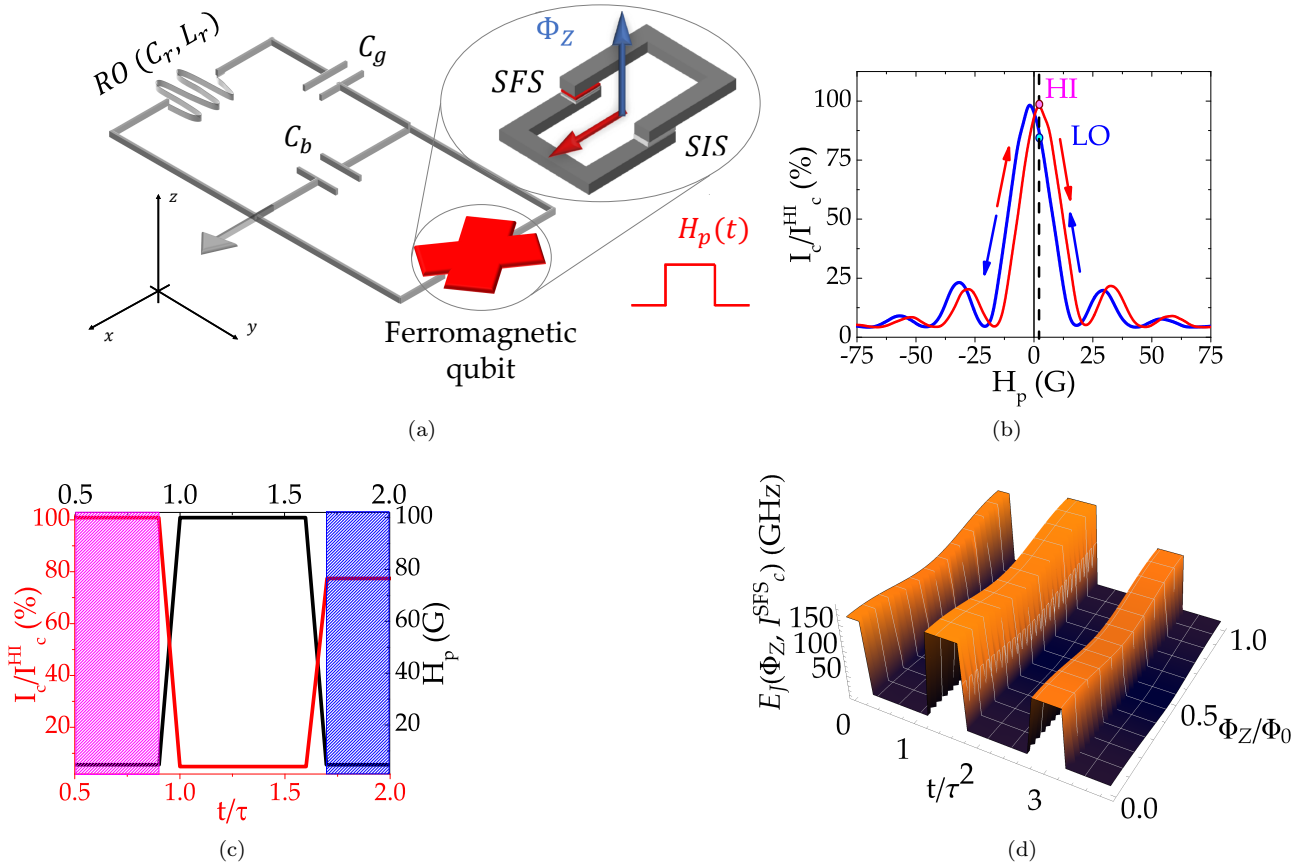


FIG. 1. In (a), ferro-transmon circuit design: the read-out (RO) resonator is capacitively coupled to the qubit through C_g . The qubit is schematized as a hybrid SQUID in parallel with a bias capacitor C_b . In the SQUID, there are a standard tunnel SIS JJ and a tunnel ferromagnetic SFS JJ. Blue and red arrows indicate magnetic fields applied along the z -axis and x -axis, respectively. In (b), $I_c(H)$ modulation in a tunnel SI_rS JJ with a 3.5 nm GdN barrier and area of $49 \mu\text{m}^2$, normalized to the maximum $I_c^{\text{HI}} = 350 \text{ nA}$. Blue and red curves in (b) refer to the down and up magnetic field pattern, respectively. We highlight in each plot the low- and high- I_c level states (LO and HI) and the working point (dashed black line). In (c), example of a magnetic field pulse sequence H_p (black line) and maximum digital tuning of the critical current I_c/I_c^{HI} (red line) for the JJ in (b). The blue and magenta dashed boxes refer to LO and HI levels, respectively. The time in (c) is normalized to a magnetic pulse timescale τ (see the text). In (d), calculated total Josephson energy E_J of a hybrid SQUID composed of a SIS JJ with $E_J^{\text{SIS}} = 10 \text{ GHz}$, i.e. $I_c^{\text{SIS}} \sim 30 \text{ nA}$, and a SI_rS JJ with GdN barrier. I_c^{SFS} is the critical current of the SFS JJ in the hybrid SQUID in (a), which is here fixed to 350 nA . The 3D-plot shows the dependence of E_J on an external flux Φ_Z (in units of the quantum magnetic flux Φ_0) and the magnetic field pulsed sequence $H_p(t)$ in (c), with time t normalized to τ .

at dilution temperatures [44], while $I_c^{\text{SIS}} \sim 30 \text{ nA}$. This also implies that far from the sweet-spots (multiple semi-integer of Φ_0), the flux-noise sensitivity of the transmon qubit is strongly reduced [14, 53].

The possibility to employ a large variety of ferromagnetic materials gives the opportunity to identify and engineer magnetic field pulses without any limitation. For instance, in the framework of Nb or NbN technology, GdN-based JJs have shown critical current variations $\Delta I = (I_c^{\text{HI}} - I_c^{\text{LO}})/I_c^{\text{HI}}$ of the order of 25% (Fig. 1 (b)). Other ferromagnetic materials employed in Nb-based JJs, such as permalloy-based JJs [37, 46] or palladium-iron PdFe-based JJs [34–36] can give ΔI of the order of 40%. Particularly relevant for PdFe barriers in SISFS JJs, ΔI can be also enhanced with the application of RF-fields [36], compatibly with standard microwave equip-

ment. Moreover, ΔI can be adjusted by designing a pulsed field sequence that exploits minor magnetization loops so to reduce the hysteresis in the $I_c(H)$ modulation, and the separation between LO and HI critical current levels [36, 37]. The magnitude of H_p does not require to reach the saturation field of the ferromagnet, which may affect the performances of the device. The working point in Fig. 1 is chosen such to have the largest separation between the LO and the HI state, ΔI . It is possible to engineer SFS JJs with finite ΔI at a working point corresponding to $H_p = 0$ [38] thus avoiding the application of external magnetic fields that may be detrimental for qubit coherence, also by employing asymmetric minor loops.

The magnetic field pulses time in Fig. 1 is normalized to a general timing of the pulsed field sequence τ , which

strongly depends on both the magnetization dynamics time-scale τ_c and the switching-speed of the tunnel-SFS JJ into play. Thus, a careful choice of the electrodynamic and magnetic properties of the tunnel-SFS JJ is fundamental to guarantee the largest speed of the digital tunability protocol. As an example, typical magnetization dynamics occurs on a time-scale $\tau_c < \text{ns}$ [54], which is far lower than the coherence times in transmon qubits range (some microsecond to hundreds of microseconds) and current state-of-the-art single- and two-qubit gate operations (tens to hundreds of nanoseconds) [4, 5, 10, 55]. The switching speed is defined by the $I_c R_N$ product of the tunnel-SFS JJ, which has already been demonstrated to be compatible with high-speed and energy-efficient superconducting digital circuits [34–37, 46], such as Single-Flux Quantum logic electronics [13, 56]. Specifically considering the NbN-GdN-NbN JJ in Fig. 1 (b), the switching speed at 10 mK is about 35 GHz, which corresponds to 28 ps. Particularly relevant for the purpose of integrating ferromagnetic materials in standard fabrication of transmon qubits without affecting their quality, in the case of SIsFS JJs the Josephson switching speed is only related to the SIs trilayer, provided that the intermediate s thickness d_s exceeds the coherence length of the superconductor ξ_s [57]. In this case, the SIsFS JJ works as a series of a standard tunnel SIs JJ and the sFS JJ [37, 46]. This ensures that: (i) the SIs JJ can be easily integrated in the transmon through standard fabrication procedures, while the F layer can be deposited afterwards without affecting the quality of the SIs trilayer, and (ii) the switching speed and the quality of the JJ are only related to the tunnel SIs JJ. The S electrode in the sFS JJ can be designed to work also as a current-line for the application of in-plane magnetic fields, which meets the request of a scalable device [38].

While on one hand the simultaneous presence of an external flux field Φ_Z and a local pulsed flux Φ_L makes this system a useful playground with multiple knobs able to tune E_J , on the other hand the proposed design allows to tune E_J only through Φ_L pulses. This means that instead of a hybrid SQUID in the qubit, it may be worth to explore also other circuitual design in which a single tunnel-SFS JJ is used, thus completely removing the effect of additional flux-noise fluctuations.

In the next section, we will discuss the role played by the electrodynamic parameters of the tunnel-SFS JJ and the capacitive couplings in the circuit design in the value of the qubit frequency, its tunability and the readout resonator dispersive shift. We focus on the estimation of the critical currents for the SFS JJs to build a reliable and measurable ferro-transmon device.

III. FEASIBILITY

The tunnel-SFS critical current I_c^{SFS} and its tuning with a local pulsed magnetic field Φ_L set the values of

the ratio E_J/E_c and the qubit frequency ω_{01} , given by

$$\omega_{01}(\Phi_Z, \Phi_L) = \sqrt{8E_{c\Sigma}E_J(\Phi_Z, \Phi_L)} - E_{c\Sigma}, \quad (4)$$

as discussed in Ref. [14] and App. A. As expected, when the ferro-transmon is coupled to a superconducting resonator, the pulsed magnetic field tuning significantly affects the effective qubit-resonator coupling and the electromagnetic response of the system. In this section, to assess the feasibility of the ferro-transmon and define the details on its circuitual design, we study its electromagnetic response in the two HI and LO states of the tunnel-SFS JJ, yielding $I_c^{\text{SFS}}(\text{HI})$ and $I_c^{\text{SFS}}(\text{LO})$.

The superconducting read-out resonator is designed as a $\lambda/4$ -coplanar waveguide with bare-frequency $\omega_{\text{RO}}^{\text{bare}} = 5.9 \text{ GHz}$ in a notch-type geometry [58]. The effective capacitance of the resonator in the lumped element approximation is $C_r = 825 \text{ fF}$ [59]. This choice has been made in order to discuss the transmon read-out for standard parameters in literature [4, 53, 60, 61]. For the same reason, we keep $E_{c\Sigma} \sim 200 \text{ MHz}$ [4, 53, 60, 61], where $E_{c\Sigma} = e^2/(2C_\Sigma)$ and C_Σ is the total effective capacitance in Eq. (A7), which depends on the coupling capacitance with the read-out resonator C_g and the qubit bias capacitor C_b in Fig. 1 (a) [14]. Finally, the qubit-readout coupling g for the first two levels of the transmon reads as [14],

$$g = g_{01} = \frac{e}{\hbar} \frac{C_g}{C_\Sigma} \sqrt{\frac{\hbar\omega_{\text{RO}}^{\text{bare}}}{C_r}} \left(\frac{E_J}{8E_c} \right)^{1/4}, \quad (5)$$

i.e. it depends on the bare-resonator frequency $\omega_{\text{RO}}^{\text{bare}}$ and the ratio between the coupling capacitance C_g and the total transmon capacitance C_Σ [14].

To explore the full range of available parameters, beside the case of a hybrid DC-SQUID dispersively coupled to a superconducting resonator, we here consider also a ferro-transmon made of a single tunnel-SFS JJ. In the latter case the tuning of the qubit frequency is achieved only through the magnetic pulsed field tuning.

A first estimation of the charging energy $E_{c\Sigma}$, the ratio E_J/E_c , the qubit frequency ω_{01} and the read-out coupling g , as a function of I_c^{SFS} and standard capacitances in the circuit, suggests the following ranges of values for the tunnel-SFS JJ critical current: (i) for I_c^{SFS} ranging from 40 to 65 nA for the hybrid DC-SQUID configuration, once set $E_{c\Sigma} = 260 \text{ MHz}$, *i.e.* $C_g = 4 \text{ fF}$ and $C_b = 70 \text{ fF}$, and I_c^{SIS} from 10 nA to 30 nA; (ii) for I_c^{SFS} ranging from 25 to 80 nA for the single tunnel-SFS JJ, once set $E_{c\Sigma} = 200 \text{ MHz}$, *i.e.* $C_g = 4 \text{ fF}$ and $C_b = 90 \text{ fF}$. These values guarantee a robust transmon regime, *i.e.* with E_J/E_c of the order of 50 – 100 [14]. Furthermore, as occurs in conventional transmon circuits based both on the Al or Nb technology, $\omega_{01} < 10 \text{ GHz}$, *i.e.* easily detected using standard qubit measurement equipment [4, 62, 63]. Charging energies above $\sim 200 \text{ MHz}$ ensure sufficiently large anharmonicity to isolate a quantum two-level system [4, 62, 63].

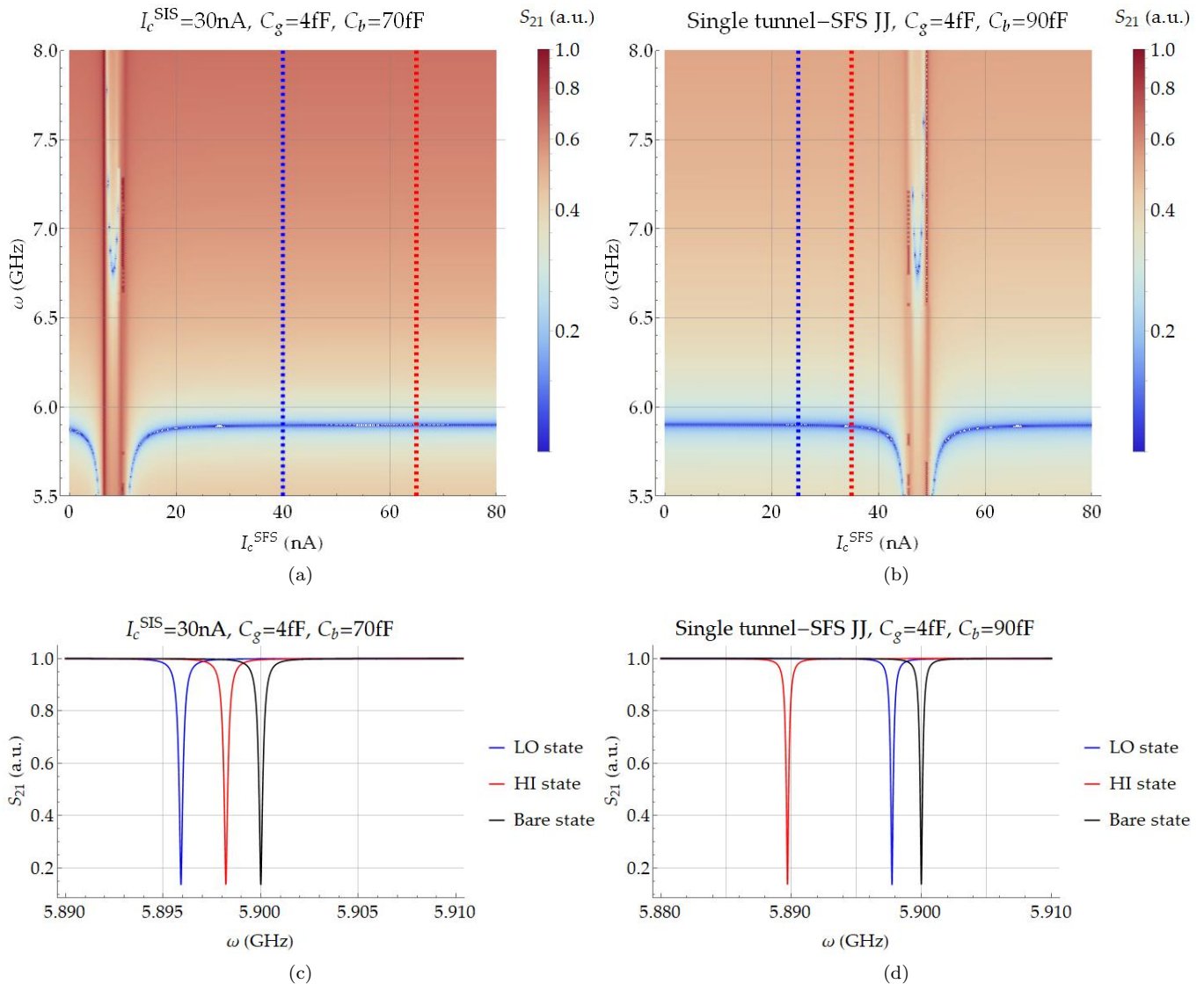


FIG. 2. Transmission parameter $S_{21}(\omega)$ in arbitrary units for the ferro-transmon read-out resonator as a function of I_c^{SFS} , the critical current in the tunnel-SFS JJ. In (a) and (b), we explore the hybrid DC-SQUID configuration, with SIS JJ critical current $I_c^{\text{SIS}} = 30 \text{ nA}$, and the ferro-transmon configuration with a single tunnel-SFS-JJ, respectively. We fix $C_b = 70 \text{ fF}$ in (a) and $C_b = 90 \text{ fF}$ in (b), and $C_g = 4 \text{ fF}$ in both the configurations. The color-scale in (a) and (b) refers to the S_{21} of a notch-type resonator in a log-scale [58], with load and coupling quality factor $Q_1 = 1.7 \cdot 10^4$ and $Q_c = 2 \cdot 10^4$, respectively, and no impedance mismatch at input and output port of the feedline. In (c) and (d), we show the readout resonator frequency dispersive shift in the high (low) level states (LO in blue and HI in red, respectively) of the SFS JJ for the configurations in panels (a) and (b), respectively. HI and LO levels in (c) and (d) are highlighted in panels (a) and (b) with the red and blue vertical dashed lines, respectively, and reported in Tab. I for completeness.

Compared to what shown in Fig. 1 (d), in which the amplitude of E_J is of the order of some hundreds of gigahertz, *i.e.* one order of magnitude larger than typical values in standard transmon devices, the reduction of I_c^{SFS} is a fundamental step in order to provide a reliable and measurable ferro-transmon device. While suitable parameters may in principle be obtained by using larger I_c^{SFS} , the $E_{c\Sigma}$ must be decreased far below 100 MHz, thus unavoidably affecting the anharmonicity of the two-level system. However, compared to the drawbacks due to a

reduction of $E_{c\Sigma}$, the I_c^{SFS} can be reduced by keeping the critical current density J_c^{SFS} constant, and therefore reducing the area of the device, or by reducing J_c^{SFS} itself.

For GdN-based JJs, for example, the J_c^{SFS} can be decreased by a factor 10 by increasing the thickness of the GdN interlayer from 3.5 nm to 4.0 nm, where typical values of 10 nA have already been reported [42, 43]. For tunnel SISFS JJs, J_c^{SFS} can be regulated changing the area of the tunnel SIS trilayer in the JJ [37]. By using strong ferromagnets such as the permalloy, for example,

the area of the JJ can be successfully scaled to dimensions of the order of some μm^2 [37], and in principle could be scaled in the sub-micrometer regime. The scaling of the area can not be accomplished, instead, on most of the soft ferromagnets used in SIsFS JJs, since they are often percolative systems or strongly dependent on a multi-domain configuration [64, 65]. However, in this case J_c^{SFS} may be reduced increasing the thickness of the insulating layer.

Finally, let us refer to the analytical approach proposed by Koch et al. in Ref. [14] to give the read-out dispersive frequency shift χ as a function of the HI and LO level states of the tunnel-SFS JJ, for both the hybrid DC-SQUID and the single tunnel-SFS JJ ferro-transmon designs. In order to work in the dispersive regime, the coupling between the read-out resonator and the qubit g in the transmon must satisfy the condition $g \ll \Delta$, where $\Delta = \omega_{\text{RO}}^{\text{bare}} - \omega_{01}$ is the detuning between the read-out resonator frequency and the first-order transition frequency for the qubit [14]. Typical coupling factors range from $g \sim 10$ MHz to 100 MHz [4, 14, 66]. In Fig. 2, we report the ideal resonator transmission parameter $S_{21}(\omega)$ [58], as a function of I_c^{SFS} ,

$$S_{21}(\omega, I_c^{\text{SFS}}) = \left| 1 - \frac{Q_1/Q_c e^{i\eta}}{1 + 2iQ_1 \left(\frac{\omega}{\omega_{\text{RO}}(I_c^{\text{SFS}})} - 1 \right)} \right|, \quad (6)$$

where $\omega_{\text{RO}}(I_c^{\text{SFS}}) = \omega_{\text{RO}}^{\text{bare}} + \chi(I_c^{\text{SFS}})$, Q_1 is the resonator total quality factor and Q_c is the coupling quality factor, fixed to $1.7 \cdot 10^4$ and $2 \cdot 10^4$, respectively [67–69]. η is the impedance mismatch at the input and output ports of the coupled feedline [58], which is here fixed to 0. Also quality factors have been chosen to comply with standard parameters in literature [58, 67–69].

We report in Fig. 2 (a) simulations for the hybrid DC-SQUID configuration with $I_c^{\text{SIS}} = 30$ nA, while in (b) we focus on the single tunnel-SFS JJ configuration. There are specific I_c^{SFS} regions for which the coupling overcomes the dispersive regime (straddling regime [4]), *i.e.* around 10 nA in panel (a) and around 50 nA in panel (b). This limits the ferro-transmon operation. In order to fall in the transmon and in the dispersive regime with feasible qubit frequency values, and to be far from the straddling regime, for the hybrid DC-SQUID configuration the best HI and LO achievable values have to be 65 nA and 40 nA, respectively. Vertical line-cuts related to these fixed I_c^{SFS} values are reported in panel (c), and compared with the transmission of the bare resonator. The same arguments can be given for the single tunnel-SFS ferro-transmon configuration in panel (b), in which we find $I_c^{\text{SFS}}(\text{HI}) = 35$ nA and $I_c^{\text{SFS}}(\text{LO}) = 25$ nA. Vertical line-cuts related to these values are reported in panel (d). A summary of the ferro-transmon electrodynamics parameters for the two configurations shown in panels (c) and (d) are finally reported in Tab. I, where we collect E_J/E_c ratio, ω_{01} , its tunability $\Delta\omega_{01} = (\omega_{01}(\text{HI}) - \omega_{01}(\text{LO}))/\omega_{01}(\text{HI})$ and the qubit-readout coupling g for the HI and LO state.

All the calculated I_c^{SFS} values are compatible with current technologies, thus making feasible the ferro-transmon. As a matter of fact, in both the proposals, the ratio E_J/E_c is comparable or larger than in typical transmon circuits. Also the qubit frequencies fall in the operational qubit frequency range [53]. Moreover, within the chosen circuital parameters, the resonator shifts χ is such to discriminate between the HI and LO state through the transmon read-out resonator in both the configurations. Most importantly, the qubit frequency tunability through a pulsed local magnetic field ranges from $\Delta\omega_Q \sim 0.8$ GHz for the single tunnel-SFS JJ to 1 GHz for the hybrid DC-SQUID configuration, as in typical flux-tunable transmons [53]. Such tunability range corresponds to $\Delta I \sim 30\%$, which can be properly engineered even by exploiting minor magnetization loops [37, 70, 71]. We stress that these parameters can be further adjusted also by changing the resonator parameters and the capacitive elements in the circuit.

IV. THE FERRO-TRANSMON AS A MAGNETIC NOISE DETECTOR

The high tunability of the ferro-transmon Hamiltonian realizes the ideal playground to study noise fluctuations in ferromagnetic Josephson devices. We show how the combined analysis of relaxation and dephasing processes in the ferro-transmon allows to characterize both magnetization fluctuations and standard flux noise. Comparing the effects of these two kinds of noise may offer important clues to optimize qubits designs and to understand fundamental aspects of quantum dissipative models.

A. Qubit-noise coupling

The ferro-transmon Hamiltonian depends on the fluxes Φ_Z and Φ_L . We assume that magnetization fluctuations yield local flux fluctuations, $\delta\Phi_L$, while Φ_Z -fluctuations, $\delta\Phi_Z$, are dominated by external electromagnetic noise, *i.e.* we neglect orbital effects of magnetization fluctuations.

The fluctuations of Φ_Z and Φ_L in turn lead to fluctuations of two classical parameters: φ_0 , defined in Appendix A, and E_J , defined by Eq. (2). To describe their effect on the qubit Hamiltonian \mathcal{H}_Q , given by Eq. (A8), we expand \mathcal{H}_Q to first order in the fluctuation amplitudes, arriving at the following expression for the ferro-transmon - noise coupling Hamiltonian $\mathcal{H}_V(t)$,

$$\mathcal{H}_V(t) = - \sum_{m=L,Z} \delta\Phi_m \left[\frac{\partial E_J}{\partial \Phi_m} \cos(\varphi - \varphi_0) + E_J \frac{\partial \varphi_0}{\partial \Phi_m} \sin(\varphi - \varphi_0) \right]. \quad (7)$$

The effect of the different contributions to $\mathcal{H}_V(t)$ can be easily understood switching to the ferro-transmon eigen-

TABLE I. Summary of the ferro-transmon parameters analyzed in this work: the charging energy $E_{c\Sigma}$, the percentual difference between the qubit frequencies in the HI (high) and LO (low) state $\Delta\omega_{01}$, the ratio E_J/E_c , the qubit frequency ω_{01} , the dispersive shift χ and the read-out coupling g , obtained following the analytical approach proposed by Koch et al. [14]. All the parameters are calculated for the hybrid DC-SQUID ferro-transmon configuration with $I_c^{\text{SIS}} = 30$ nA (a), and for a ferro-transmon with a single SFS-JJ (b). Each of the configurations is characterized by $C_g = 4$ fF, while C_b is 70 fF for the former, and 90 fF for the latter.

	(a) $I_c^{\text{SIS}} = 30$ nA		(b) Single tunnel-SFS JJ	
	HI : $I_c^{\text{SFS}} = 65$ nA	LO: $I_c^{\text{SFS}} = 40$ nA	HI : $I_c^{\text{SFS}} = 35$ nA	LO: $I_c^{\text{SFS}} = 25$ nA
$E_{c\Sigma}$ (MHz)	261		205	
$\Delta\omega_{01}$ (%)	15		16	
E_J/E_c	179	132	84	61
ω_{01} (GHz)	9.66	8.25	5.13	4.30
$ \chi $ (MHz)	1.79	4.09	10.72	2.36
g (MHz)	82	98	91	61

state basis. In this basis, keeping only the first two levels and assuming $E_J(\Phi_Z, \Phi_L) \gg E_{c\Sigma}$, we can write $\mathcal{H}_Q \simeq \omega_{01}\sigma_z$, with $\omega_{01} = \omega_Q(\Phi_Z, \Phi_L) - E_{c\Sigma}$ and

$$\mathcal{H}_V(t) \simeq -\sum_{m=L,Z} [A_{m\parallel}\sigma_z + A_{m\perp}\sigma_y] \frac{\pi\delta\Phi_m}{\Phi_0}, \quad (8)$$

where $A_{m\parallel}$ and $A_{m\perp}$ are respectively given by

$$A_{m\parallel} = \frac{\Phi_0}{2\pi} \sqrt{\frac{8E_{c\Sigma}}{E_J}} \frac{\partial E_J}{\partial \Phi_m} \quad (9)$$

and

$$A_{m\perp} = \frac{E_J\Phi_0}{\pi} \left[2 \left(\frac{2E_{c\Sigma}}{E_J} \right)^{1/4} - \left(\frac{2E_{c\Sigma}}{E_J} \right)^{3/4} \right] \frac{\partial \varphi_0}{\partial \Phi_m}. \quad (10)$$

Starting from Eqs. (8)-(10) and employing Bloch-Redfield theory [72], we see that, as expected, fluctuations of E_J yield qubit's dephasing, while fluctuations of the phase φ_0 lead to relaxation. Therefore, since both $\delta\Phi_Z$ and $\delta\Phi_L$ induce both φ_0 and E_J fluctuations, either of them yields both dephasing and relaxation.

In particular, the fluctuations of the local flux $\delta\Phi_L$ can be related to H_p and M fluctuations. Using Eq. (1), $\delta\Phi_L$ can be indeed cast as follows

$$\delta\Phi_L = d_m a \delta H_p + 4\pi d_F a \delta M. \quad (11)$$

Here, δM and δH_p are not independent. However, by assuming an instantaneous response of the ferromagnet to the pulsed magnetic field fluctuations, we can write

$$\delta M(t) = \chi \delta H_p(t) + \delta M_i(t) \quad (12)$$

where χ denotes the ferromagnet's susceptibility and δM_i indicates the fluctuations of the magnetization at $H_p = 0$ i.e. such that $\langle \delta M_i \delta H_p \rangle = 0$. The assumption of instantaneous response is justified for the purpose of calculating the rates if the ferromagnet magnetization dynamics is faster than the magnetic field pulse sequence time-scale and the qubit's dynamics.

In the following starting from the above equations we calculate the relaxation rates and the dephasing characteristic and we show that it is possible to isolate the effects of the different noise sources at specific working points.

B. Relaxation

The total decay rate due to relaxation/excitation processes is given by $\Gamma_1 = \Gamma_\downarrow + \Gamma_\uparrow$, where relaxation (excitation) Γ_\downarrow (Γ_\uparrow) rates in terms of the spectral noise function read as

$$\Gamma_\downarrow = \sum_{m=L,Z} A_{m\perp}^2 S_{\Phi_m}(\omega_{01}) \frac{\pi^2}{\Phi_0^2} \quad (13)$$

$$\Gamma_\uparrow = \sum_{m=L,Z} A_{m\perp}^2 S_{\Phi_m}(-\omega_{01}) \frac{\pi^2}{\Phi_0^2}, \quad (14)$$

where $S_X(\omega)$ denotes the noise spectral function at frequency ω , $S_X(\omega) = \int \langle X(t)X(0) \rangle e^{i\omega t} dt$. Specifically, using Eq. (12), $S_{\Phi_L}(\omega)$ can be written as follows

$$S_{\Phi_L}(\omega) = \beta_1^2 S_{H_p}(\omega) + (4\pi\beta_2)^2 S_{M_i}(\omega), \quad (15)$$

where $\beta_1 = d_m a (1 + \frac{d_F}{d_m} \chi)$ and $\beta_2 = d_F a$. To estimate S_{Φ_Z} , we follow Refs. [14, 75, 84], and we consider both the Ohmic and the $1/f$ contributions, respectively denoted as $S_{\Phi_Z}^{\text{Ohmic}}$ and $S_{\Phi_Z}^{1/f}$. The former is estimated as [14, 75]

$$S_{\Phi_Z}^{\text{Ohmic}} = L_m^2 S_{I_n}(\omega_{01}), \quad (16)$$

where L_m indicates the mutual inductance between the SQUID and the flux-bias loop, and S_{I_n} denotes the current noise spectrum in the flux bias circuit. The $1/f$ contribution is modelled as suggested in Ref. [84] as:

$$S_{\Phi_Z}^{1/f} = A_{\Phi_Z}^2 \left(2\pi \frac{1 \text{ Hz}}{\omega} \right)^{0.9}, \quad (17)$$

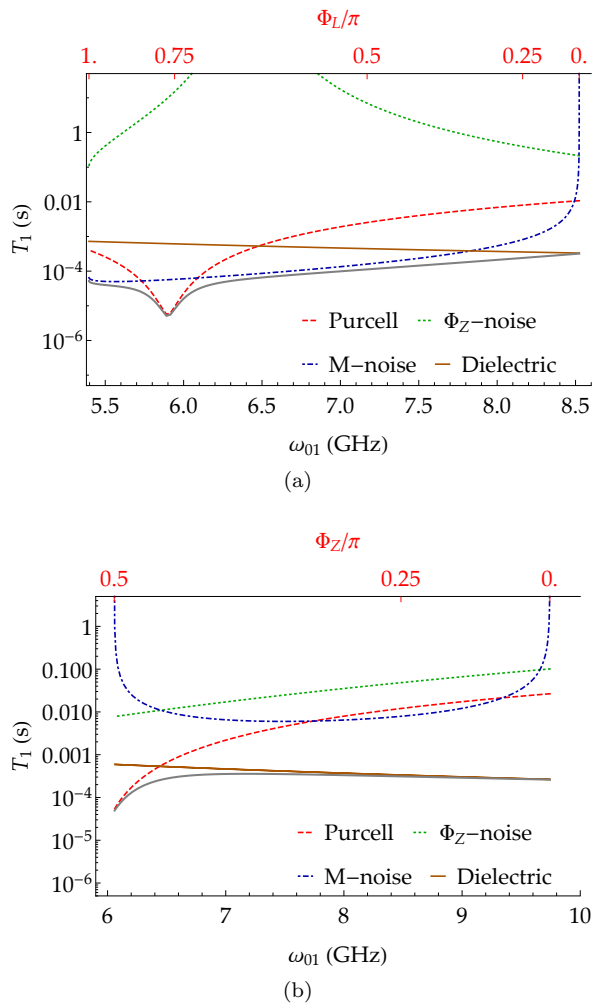


FIG. 3. Relaxation time T_1 due to Purcell (red dashed curve) and dielectric (orange curve) effects, magnetization (blue dashed-dotted curve) and flux noise (green dotted curve) fluctuations for the ferro-transmon in the hybrid DC-SQUID configuration as a function of the qubit frequency ω_{01} for $g = 80$ MHz, $E_J^{\text{SFS}}(\text{HI}) = 32$ GHz, $E_J^{\text{SIS}}(\text{HI}) = 14$ GHz, $E_c = 260$ MHz, $\kappa = 400$ kHz, $\tau_c = 1$ ps. In (a), we fix $\phi_Z = \pi/4$ and we change $\phi_L \in [0, \pi]$, while in (b) we fix $\phi_L \sim \pi/12$ and we change $\phi_Z \in [0, \pi/2]$. The grey curve represents the total relaxation time T_1 , given by the sum of all the relaxation contributions.

with $A_{\Phi_Z} = 1.4\mu\phi_0$. As illustrated in Ref. [84], at frequencies of the order of ω_{01} , the $1/f$ contribution dominates over the Ohmic one due to the smallness of the inductance L_m .

In the low-temperature limit $k_B T \ll \hbar\omega_{01}$, the above equations eventually allow us to recast the decay rate as the sum of three contributions, *i.e.* $\Gamma_1 = \Gamma_{1,\Phi_Z} + \Gamma_{1,H_p} + \Gamma_{1,M_i}$ where Γ_{1,H_p} accounts for the fluctuations of the pulsed magnetic field,

$$\Gamma_{1,H_p} \simeq A_{L\perp}^2 \beta_1^2 S_{H_p}(\omega_{01}) / (4\Phi_0^2), \quad (18)$$

Γ_{1,M_i} accounts for the fluctuations of the magnetization

$$\Gamma_{1,M_i} \simeq A_{L\perp}^2 (4\pi\beta_2)^2 S_{M_i}(\omega_{01}) / (\Phi_0^2) \quad (19)$$

and Γ_{1,Φ_Z} is associated to the fluctuations of the flux Φ_Z ,

$$\Gamma_{1,\Phi_Z} \simeq A_{z\perp}^2 (S_{\Phi_Z}^{\text{Ohmic}} + S_{\Phi_Z}^{1/f}) / \Phi_0^2. \quad (20)$$

Interestingly, at $H_p \equiv 0$, the contributions of M_i and Φ_Z can be isolated by appropriately choosing the qubit's working point. Indeed, according to Eq. (10), the coupling of M_i and Φ_Z fluctuations are proportional to the derivatives $\partial\varphi_0/\partial\Phi_L$ and $\partial\varphi_0/\partial\Phi_Z$, respectively. The latter have the following expressions in terms of the Josephson energy E_J^{SFS} and the asymmetry parameter d ,

$$\frac{\partial\varphi_0}{\partial\Phi_L} = \frac{1}{4} \frac{(1-d^2)\sin(2\phi_Z)}{\cos^2(\phi_Z) + d^2\sin^2(\phi_Z)} \frac{\partial \log E_J^{\text{SFS}}}{\partial\phi_L} \quad (21)$$

$$\frac{\partial\varphi_0}{\partial\phi_Z} = \frac{d^2}{\cos^2(\phi_Z) + d^2\sin^2(\phi_Z)}, \quad (22)$$

with $\phi_m = \pi\Phi_m/\Phi_0$, and $m = \{L, Z\}$. We see that for $d \sim 0$, it is possible to suppress $\partial\varphi_0/\partial\phi_Z$, and the relaxation rate can be directly related to the intrinsic magnetization noise spectrum $S_{M_i}(\omega_{01})$. On the contrary, at $\phi_Z = 0$ and $d \neq 0$, the relaxation rate yields indications on $S_{\Phi_Z}(\omega_{01})$. Clearly, other relaxation channels such as Purcell effect, dielectric losses and quasi-particle relaxation may contribute to Γ_1 and hinder the measurement of magnetic fluctuation noise.

To illustrate this point, in Fig. 3 we compare the relaxation induced by magnetization and flux fluctuations, dielectric losses and Purcell effect by plotting the corresponding relaxation times. In order to calculate the relaxation rates associated with magnetization and flux noise in Fig. 3, we use Eqs. (19-20) and we estimate the spectral function $S_{\Phi_Z}(\omega_{01})$ using Eq. (16), *i.e.* we consider ohmic and $1/f$ -type Φ_Z -fluctuations [14]. Instead, for the spectral function $S_{\Phi_L}(\omega_{01})$ we assume that: (i) the amplitude of the magnetization fluctuations satisfy the relation $\delta M_i \lesssim 5 \cdot 10^{-3} M_{\text{sat}}$, with M_{sat} the saturation magnetization of the ferromagnet, and (ii) the magnetization correlation function decays exponentially on a time scale $\tau_c \sim 1$ ps $< \tau$, where τ is the magnetic field pulse sequence time-scale. The corresponding noise spectrum reads as:

$$S_{\Phi_L}(\omega) = \delta M_i^2 \tau_c / (\tau_c^2 \omega^2 + 1). \quad (23)$$

As reported in Ref. [73], capacitive losses relaxation contribution Γ_{1c} are defined as:

$$\Gamma_{1c} = \frac{2}{\hbar} |\langle 0|2eN|1\rangle|^2 \frac{1}{CQ(\omega_{01})}, \quad (24)$$

where C is the lossy capacitance of the superconducting island in the transmon, with quality factor $Q(\omega) =$

$\text{Im}Y_{\text{cap}}(\omega)/\text{Re}Y_{\text{cap}}(\omega)$, defined in terms of the capacitance admittance $Y_{\text{cap}}(\omega)$ [73]. Therefore, a crucial role is played by the superconducting and dielectric materials involved in the circuit. In the following, we will refer to standard parameters reported in literature [22, 32, 73].

Finally, to describe Purcell relaxation across different regimes we use the expression given *e.g.* in Ref. [74],

$$\Gamma_{1\text{Purcell}} = \frac{\kappa}{2} \left(1 - \frac{\Delta^2}{\Delta^2 + 4g^2} \right), \quad (25)$$

where $\kappa = \omega_{\text{RO}}/Q_c$ is the resonator decay rate, Δ is the qubit-resonator detuning and g is the qubit-resonator coupling.

In Fig. 3 (a) and (b), we show the total relaxation time $T_1 = 1/\Gamma_1$ and the relaxation times corresponding to the magnetization and flux fluctuations, dielectric losses and Purcell noise, respectively given by $1/\Gamma_{1,M_i}$, $1/\Gamma_{1,\Phi_Z}$, $\Gamma_{1,c}$ and $1/\Gamma_{1\text{Purcell}}$, as a function of the ferro-transmon qubit frequency ω_{01} . In Fig. 3 (a), ω_{01} is varied by tuning the local flux field Φ_L (red axis in the panel) and setting $\Phi_Z = \Phi_0/4$, while in Fig. 3 (b) it is varied by tuning Φ_Z and setting $\Phi_L = \Phi_0/12$.

We see that by properly choosing the flux and local field working point, the ferro-transmon might be used as a magnetic noise detector. For example, in Fig. 3 (a) magnetization fluctuations are the dominant relaxation channel in a wide range of local flux field below $\Phi_L = 0.4\pi$, with the exception of a narrow region occurring for resonant qubit-resonator coupling, where the Purcell effect is the dominant relaxation channel. Above $\Phi_L = 0.4\pi$, instead, dielectric losses are the dominant relaxation processes.

Analogously, dielectric losses are also dominant in Fig. 3 (b) in the whole frequency range. Thus, while magnetization fluctuations can be evaluated by measuring the ferro-transmon relaxation rate, flux-noise fluctuations are expected to be small compared to other relaxation channels [14]. However, it has been demonstrated that a careful choice of the materials into play can minimize this effect, thus allowing to highlight Φ_Z -induced relaxation [9] for specific values of $\Phi_Z \sim 0$ as predicted by Eq. (22).

C. Dephasing

To describe the dephasing behavior, we start by expressing the density-matrix ρ_{01} in terms of δM_i , δH_p and $\delta \Phi_Z$ by using Eq. (11). Within the assumption of Gaussian noise [75] and free-evolution, it reads as

$$\rho_{01}(t) = \rho_{01}(0) e^{i\omega_{01}t} \exp \left[-\frac{A_{Z\parallel}^2}{8\Phi_0^2} \left\langle \left(\int_0^t \delta \Phi_Z \right)^2 \right\rangle \right] \cdot \exp \left[-\frac{A_{L\parallel}^2}{8\Phi_0^2} \left\langle \left(\int_0^t \beta_1 \delta H_p + 4\pi\beta_2 \delta M_i \right)^2 \right\rangle \right] \quad (26)$$

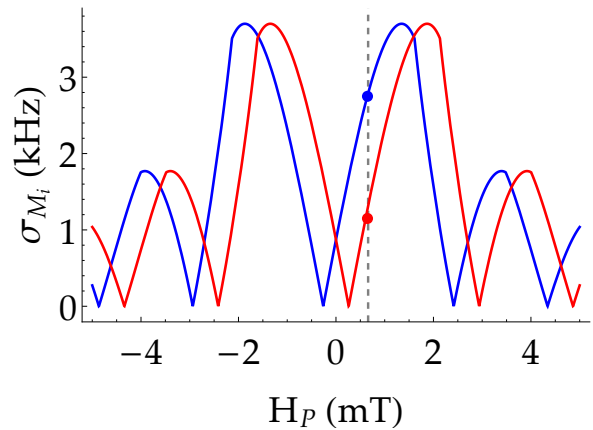


FIG. 4. Gaussian decay rate σ_{M_i} (Eq. (29)) along the up and down magnetization curves as a function of the local magnetic field. The red and blue dots correspond to $E_J^{\text{SFS}} = 32$ GHz and $E_J^{\text{SFS}} = 20$ GHz and we set $E_c = 0.261$ GHz, $E_J^{\text{SIS}} = 15$ GHz and $A_{M_i} \sim 1 \mu\text{T}$. The dependence of E_J^{SFS} on the magnetic field is estimated from the Fraunhofer-like curves given in Fig. 1 (b).

where we assumed $\langle \delta \Phi_Z \delta \Phi_L \rangle = 0$. The decay characteristic of the qubit dictated by this equation depends sensitively on the noise source spectrum. Specifically, setting $\langle \delta H_p \delta M_i \rangle = 0$ and introducing the functions $f_\lambda(t) = \int_{-\infty}^{\infty} S_\lambda(\omega) \frac{\sin^2(\omega t/2)}{(\omega/2)^2} d\omega$ with $\lambda = \{M_i, H_p, \Phi_Z\}$, we can write

$$\rho_{01}(t) = \rho_{01}(0) e^{i\omega_{01}t} \exp \left[-\frac{A_{Z\parallel}^2}{8\Phi_0^2} f_{\Phi_Z}(t) \right] \cdot \exp \left[-\frac{A_{L\parallel}^2}{8\Phi_0^2} \left(\beta_1^2 f_{H_p}(t) + (4\pi\beta_2)^2 f_{M_i}(t) \right) \right]. \quad (27)$$

In order to calculate the functions $f_\lambda(t)$ we need information on the typical time scales of the system and of the noise sources. Low-frequency magnetic flux noise in superconducting qubits typically has a $1/\omega^\nu$ with $\nu \in [0.7, 1.2]$ and it may be affected by a wide range of factors, including fabrication details, materials properties as well as the structure of the junction and the circuit [75]. Analogously, spontaneous magnetization fluctuations in a ferromagnet due to domain wall dynamics, trapped ions and defect at the ferromagnet surface [76–78] may display different spectral behaviors, such as a $1/\omega$ frequency dependence as reported in Refs. [79, 80] or a $1/\omega^\nu$ with $\nu = 3/2$ as recently demonstrated by Balk et al. in Ref. [81]. We start by deriving a general analytical expression for the decay of ρ_{01} considering only the effect of magnetization fluctuations. We here assume that

$$S_{M_i}(\omega) = A_{M_i}^2/\omega \cdot (\omega_0/\omega)^{\nu-1} \quad \text{for } \omega \in [\omega_{\text{ir}}, \omega_{\text{uv}}], \quad (28)$$

where ω_{ir} and ω_{uv} are the infrared and ultra-violet cutoff, respectively. We also assume that the typical evolution time t satisfies $\omega_{\text{uv}}^{-1} < t < \omega_{\text{ir}}^{-1}$ and $1/2 \leq \nu \leq 3/2$

following Refs. [82, 83]. Starting from the spectrum of Eq. (28), the integral in Eq. (27) can be easily calculated numerically as shown in App. B. Thus, we can derive simple analytic approximations for $\rho_{01}(t)$. Specifically, for $\nu = 1$ we obtain

$$\rho_{01}(t) \propto e^{-(\sigma_{M_i}^2 t^2) \ln(\pi/(\omega_{ir}t))} \quad \text{with} \quad \sigma_{M_i} \simeq A_{L\parallel} \frac{\pi\beta_2 A_{M_i}}{\Phi_0}, \quad (29)$$

while for $\nu \neq 1$ we can write $\rho_{01}(t) \propto \exp^{-\sigma_{M_i}^2 t^2 \alpha_\nu(t)}$ with

$$\alpha_\nu(t) = \frac{1 - (\omega_{ir}t/\pi)^{\nu-1}}{\nu - 1} \left(\frac{\omega_0}{\omega_{ir}} \right)^{\nu-1}, \quad (30)$$

valid for $\omega_{ir}t \ll 1$.

For the other sources of $1/f$ noise we can make similar reasoning and obtain analogous results, *i.e.* taking into account the different coupling constants we can write:

$$\sigma_{H_L} \simeq A_{L\parallel} \frac{\pi\beta_1 A_{H_L}}{\Phi_0} \quad \text{and} \quad \sigma_{\Phi_Z} \simeq A_{Z\parallel} \frac{\pi A_{\Phi_Z}}{\Phi_0}, \quad (31)$$

assuming for both noise sources $\nu = 1$. For Φ_Z -noise a more precise description of the behavior of the spectral function can be given by Eq. 17 [84].

For $\omega \in [\omega_{ir}, \omega_{uv}]$, where ω_{ir} and ω_{uv} may be different for the different noise sources, we made the following assumptions on the external flux and local magnetic field fluctuations:

$$S_{H_L}(\omega) = A_{H_L}^2 / \omega \cdot (\omega_0/\omega)^{\nu-1} \quad (32)$$

and

$$S_{\Phi_Z}(\omega) = A_{\Phi_Z}^2 / \omega \cdot (\omega_0/\omega)^{\nu-1}. \quad (33)$$

Such low-frequency behavior of magnetic spectral functions is encoded in the dephasing characteristic and can be accessed by Ramsey and echo experiments [14]. Also in this case, the contributions of magnetization and Φ_Z fluctuations can be separated. Indeed at the external flux sweet spots located at $\phi_Z = n\pi$ as in standard transmons, the dephasing is mostly due to intrinsic magnetization fluctuations, while the effect of external magnetic field fluctuations is negligible. On the other hand, for $\phi_Z \neq n\pi$ and ϕ_L tuned at the local flux sweet spots, $\Phi_L = \Phi_L^*$, ferro-transmon's dephasing probes Φ_Z 's fluctuations. Notice that the local flux sweet spots, defined by the condition $\left. \frac{\partial E_J^{\text{SFS}}}{\partial \Phi_L} \right|_{\Phi_L = \Phi_L^*} = 0$, depend on the properties of the SFS JJ.

Also in the case of dephasing rates, we can roughly estimate their order of magnitude. In Fig. 4, we plot the behavior of the gaussian decay rate for the intrinsic magnetic fluctuations σ_{M_i} , as given by Eq. (29), and as a function of the local magnetic field. σ_{M_i} has been obtained by fitting with a Fraunhofer-like pattern the up and down $I_c(H_p)$ curves in Fig. 1 (b), and rescaled in order to achieve the suitable E_J^{SFS} in Fig. 2 (a). The red and blue dots in Fig. 4 indicate two possible HI and

LO working points corresponding to the red and blue resonances spectra shown in Fig. 2 (c), respectively. As discussed in Sec. II, in principle, we can adapt the pulsed magnetic field sequence in order to reach the largest decay time due to magnetization fluctuation dephasing.

D. Noise detection protocol

The analysis of the effect of different noise sources on the ferro-transmon design allows to propose a novel protocol for the study of the spectral noise functions in hybrid ferromagnetic quantum systems. In Fig. 5 we highlight how we can access to Φ_Z and M_i noise spectra. In the first phase, a basic characterization of the qubit is in order to obtain information on the sweet-spots in presence of Φ_Z , the maximum of the E_J in presence of Φ_L and the points at which the asymmetry between the SIS and the SFS JJs in the loop is zero. This is a fundamental step also for extracting the π -pulse for the study of relaxation and the dephasing processes in the system. In the second phase, we propose to perform T_1 measurements in two configurations: (i) at $d = 0$ and $\Phi_Z \neq 0$ to address high-frequency magnetization-noise spectra, and (ii) for asymmetry $d \neq 0$ and $\Phi_Z = 0$ to address high-frequency Φ_Z -noise spectra. The third step involves standard Ramsey and Echo sequence in other two configurations: (i) at the sweet-spots for Φ_Z -noise spectra to address low-frequency M_i -noise spectra and (ii) in the maximum of the Fraunhofer-like modulation of the Josephson energy to address low-frequency Φ_Z -noise. We remark that the simultaneous measurement of relaxation and dephasing is also extremely relevant to fully characterize $1/f$ noise, as demonstrated in various works [83–85].

V. CONCLUSIONS

The natural digital behavior of SFS JJs and the recent advancements in fabrication of high-quality and low-dissipative tunnel SFS JJs give the possibility to implement hybrid quantum devices compatible with energy-efficient cryogenic digital electronics. We have discussed the capabilities and the feasibility of a ferro-transmon that uses a hybrid ferromagnetic SQUID coupled to a superconducting resonator, thus giving a first estimation of the electrical and magnetic parameters needed to fabricate a reliable and measurable device. By considering capacitive elements in the circuit design in line with typical values already implemented in non-magnetic transmon devices, we demonstrated the feasibility of the proposed circuit. The insertion of a ferromagnetic barrier in a JJ allows for the investigation of new problems due to the interplay between the two competing superconducting and ferromagnetic order parameters [24, 27]. Beside its potential for quantum computing applications, a hybrid ferromagnetic qubit in turn offers the possibility to study the dynamics of the tunnel-SFS JJ itself, yielding novel

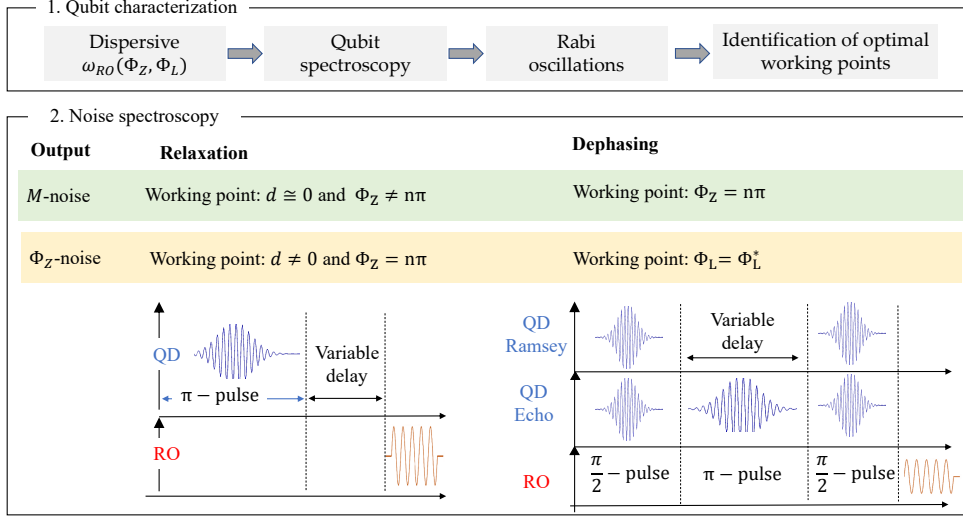


FIG. 5. Measurement protocol for the investigation of low- and high-frequency spectral noise functions of the intrinsic magnetic fluctuations (green boxes) and external magnetic field fluctuations (orange boxes). The protocol is divided into two phases: phase (1) regards standard qubit characterization; phase (2) summarizes the study of relaxation phenomena through relaxation time measurements and dephasing time measurements for noise spectroscopy. In phase (2) we also report standard microwave pulsed sequences for the qubit drive (QD) and the read-out (RO) for the relaxation, Ramsey and Echo sequences, respectively [4].

experimental tools to probe quantum phenomena at the interface. We demonstrate that investigating qubit’s dephasing and relaxation at suitable working points it is possible to probe both magnetization fluctuations and magnetic flux noise.

ACKNOWLEDGMENTS

The work has been supported by the project “EffQul - Efficient integration of hybrid quantum devices” - Ricerca di Ateneo Linea A, CUP: E59C20001010005 and the project “SQUAD - On-chip control and advanced read-out for superconducting qubit arrays”, Programma STAR PLUS 2020, Finanziamento della Ricerca di Ateneo, University of Napoli Federico II. This work was also co-funded by European Union - PON Ricerca e Innovazione 2014-2020 FESR/FSC - Project ARS01_00734 QUANCOM. H.G.A., D.M., D. Mo. and F.T. thank NANOCOBYBRI project (COST Action CA 16218). The authors also thank Mark G. Blamire and Avradeep Pal for useful discussions.

CONFLICT OF INTEREST

The authors declare that they have no conflict of interest.

Appendix A: Ferro-transmon Hamiltonian

We here highlight the derivation of the ferro-transmon charging Hamiltonian. Following the standard approach discussed e.g. in Ref. [72] we can easily derive the charging Hamiltonian of the ferro-transmon starting from its Lagrangian:

$$\mathcal{L}_c(\dot{\Phi}_r, \dot{\Phi}) = \frac{C_r \dot{\Phi}_r^2}{2} + \frac{C_b \dot{\Phi}^2}{2} + \frac{C_g}{2} (\dot{\Phi}_r - \dot{\Phi})^2. \quad (\text{A1})$$

where Φ_r and Φ denote respectively the resonator and qubit node fluxes.

Starting from the above equation, we can obtain an expression for the charging Hamiltonian written in term of the charges Q_r and Q , conjugate to the fluxes Φ_r and Φ , and defined as usual as $Q_i = \partial_{\dot{\Phi}_i} \mathcal{L}_c(\dot{\Phi}_i)$. By doing so, we obtain $\mathbf{Q} = \hat{M}^{-1} \dot{\Phi}$, with \hat{M}^{-1} denoting the capacitance matrix

$$\hat{M}^{-1} = \begin{pmatrix} C_r + C_g & -C_g \\ -C_g & C_b + C_g \end{pmatrix}, \quad (\text{A2})$$

and

$$\mathcal{H}_c = \frac{1}{2} \mathbf{Q} \hat{M} \mathbf{Q}. \quad (\text{A3})$$

By inverting the capacitance matrix, we can thus directly obtain information on the interplay between the capacitive elements in the circuit and their effect on the total energy of the system [14]. Let us now discuss more in

details the different contributions to the ferro-transmon Hamiltonian.

Given the small dimensions of standard transmon devices ($\sim 100 \mu\text{m}^2$) [51, 52], the transmission line resonator in the circuit can be described by a harmonic LC oscillator in the lumped element limit. Hence, the resonator Hamiltonian H_r reads as

$$\mathcal{H}_r = \frac{Q_r^2}{2C_{\Sigma_r}} + \frac{\Phi_r^2}{2L_r}, \quad (\text{A4})$$

where C_{Σ_r} is the effective total capacitance of the resonator circuit net, which depends on all the capacitance of the circuits, and reduces to C_r in the limit $C_r \gg C_b, C_g$ [14]. The coupling between the qubit and the resonator, $\mathcal{H}_{\text{coupl}}$, can be cast as

$$\mathcal{H}_{Q-r} = \frac{QQ_r}{2C_{\Sigma_{\text{Coupl}}}}, \quad (\text{A5})$$

where Q is the excess charge in the SQUID circuit and $C_{\Sigma_{\text{Coupl}}}$ is the total effective coupling capacitance. These two terms are the same as occurs in standard transmon devices, and derivation of their explicit expressions can be found in Ref. [14].

The qubit Hamiltonian \mathcal{H}_Q can be written as

$$\mathcal{H}_Q = \frac{Q^2}{2C_\Sigma} - E_J^{\text{SIS}} \cos \varphi_1 - E_J^{\text{SFS}}(\Phi_L) \cos \varphi_2 \quad (\text{A6})$$

where φ_1 and φ_2 are the phase differences across the SIS and SFS junctions respectively, E_J^{SIS} and E_J^{SFS} are the corresponding Josephson couplings and C_Σ is the total effective capacitance obtained from Eq. (A3),

$$C_\Sigma = \frac{(C_g + C_b)C_r + C_g C_b}{C_r + C_g}. \quad (\text{A7})$$

Assuming negligible inductance of the SQUID loop we can set $\varphi_1 - \varphi_2 = 2\pi\Phi_Z/\Phi_0$, Φ_0 denoting the elementary flux, and we can recast the Hamiltonian \mathcal{H}_Q as

$$\mathcal{H}_Q = \frac{Q^2}{2C_\Sigma} - E_J(\Phi_Z, \Phi_L) \cos(\varphi - \varphi_0), \quad (\text{A8})$$

where $\varphi = \varphi_1 + \varphi_2$, and $E_J(\Phi_Z, \Phi_L)$ is defined in Eq. (2) in terms of the local pulsed flux Φ_L and the external flux Φ_Z . The phase-shift φ_0 also depends on Φ_L and the external flux Φ_Z through the asymmetry parameter in Eq. (3), and reads as

$$\tan \varphi_0(\Phi_Z, \Phi_L) = -d(\Phi_L) \tan \Phi_Z. \quad (\text{A9})$$

In the transmon regime, $E_J(\Phi_Z, \Phi_L) \gg E_{c\Sigma}$, \mathcal{H}_Q reduces to the following Duffing Harmonic oscillator Hamiltonian [86]

$$\mathcal{H}_Q \simeq \hbar\omega_Q(\Phi_Z, \Phi_L) \left(b^\dagger b + \frac{1}{2} \right) - \frac{E_{c\Sigma}}{12} (b + b^\dagger)^4, \quad (\text{A10})$$

where b (b^\dagger) are the annihilation (creation) operators, whose definition follows the standard notation introduced

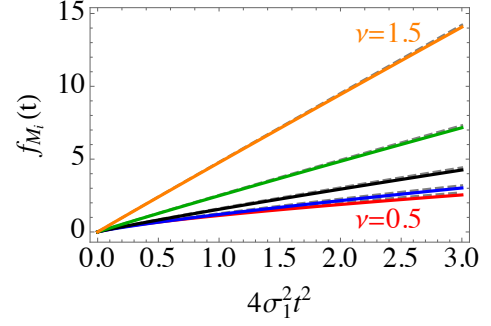


FIG. 6. Behavior of the decaying exponent of $\rho_{01}(t)$ for different $1/f$ noise's exponents $\nu = 1.5, 1.25, 1, 0.75, 0.5$ and infrared $\omega_{\text{ir}} = 0.01 \omega_0$. The gray dashed lines represent the corresponding analytic approximations defined by Eqs. (29)-(30).

in Ref. [14], $\omega_Q(\Phi_Z, \Phi_L)$ is the qubit frequency in the harmonic approximation, defined as

$$\omega_Q(\Phi_Z, \Phi_L) = \sqrt{8E_J(\Phi_Z, \Phi_L)E_c}, \quad (\text{A11})$$

and the quartic term in Eq. (A10), yielding the anharmonicity, depends only on the circuit's charging energy [14],

$$E_{c\Sigma} = \frac{e^2}{2C_\Sigma}. \quad (\text{A12})$$

For tunnel SFS JJs, the capacitance is the same order of magnitude of that in non-magnetic tunnel JJs [41, 43, 87]. As a consequence, the charging energy of the circuit is mostly unaffected by the presence of the SFS JJ, and the main difference between the ferro-transmon and a standard transmon circuit is related to the Josephson energy, as discussed in Sec. II.

Appendix B: Analytic approximations for the ferro-transmon-noise couplings and the decay characteristics

We outline here the derivation of Eqs. (9)-(10). Starting from the Hamiltonian (7) one easily realizes that in the truncated basis the ferro-transmon noise couplings will be determined by the following matrices:

$$\begin{aligned} \hat{A}_{mn} &= \langle \psi_m | \cos(\varphi - \varphi_0) | \psi_n \rangle \\ \hat{B}_{mn} &= \langle \psi_m | \sin(\varphi - \varphi_0) | \psi_n \rangle \end{aligned} \quad (\text{B1})$$

with $|\psi_n\rangle$ with $n = 0, 1$ representing the lowest transmon eigenfunctions. The matrices \hat{A} and \hat{B} can be calculated employing the harmonic approximation as follows

$$\hat{A}_{mn} \simeq \hat{A}_{mn}^H = \langle \psi_m^H | \frac{(\varphi - \varphi_0)^2}{2} | \psi_n^H \rangle$$

and

$$\hat{B}_{mn} \simeq \hat{B}_{mn}^H = \langle \psi_m^H | \left[(\varphi - \varphi_0) + \frac{(\varphi - \varphi_0)^3}{6} \right] | \psi_n^H \rangle.$$

Using these approximated expressions in Eq. (7) and using Eq. (8) we can then write

$$A_{m\perp} = \text{Tr} \left[\hat{B}^H \sigma_x \right] \quad \text{and} \quad A_{m\parallel} = \text{Tr} \left[\hat{A}^H \sigma_z \right],$$

and we can recover Eqs. (9)-(10) by a simple calculation.

To conclude this section we report in Fig. 6 the decay-exponent f_{M_i} of $\rho_{01}(t)$,

$$\rho_{01}(t) = \rho_{01}(0) e^{i\omega_{01}t} e^{-f_{M_i}(t)}, \quad (\text{B2})$$

as a function of t^2 for different values of the $1/f$ noise sources exponent ν . The gray dashed lines in Fig. 6 represent the analytic approximations that are in good agreement with the numerical results. As explained in Sec. IV, the determination of the exponent ν for different noise sources can be done by combined relaxation and dephasing measurements at suitable working points.

-
- [1] J. Clarke and F. K. Wilhelm, Superconducting quantum bits, *Nature* **453**, 1031 (2008).
- [2] M. H. Devoret and R. J. Schoelkopf, Superconducting circuits for quantum information: an outlook, *Science* **339**, 1169 (2013).
- [3] A. F. Kockum and F. Nori, Quantum bits with Josephson junctions, in *Fundamentals and Frontiers of the Josephson Effect*, edited by F. Tafuri (Springer International Publishing, Cham, 2019) pp. 703–741.
- [4] P. Krantz, M. Kjaergaard, F. Yan, T. P. Orlando, S. Gustavsson, and W. D. Oliver, A quantum engineer’s guide to superconducting qubits, *Applied Physics Reviews* **6**, 021318 (2019), <https://doi.org/10.1063/1.5089550>.
- [5] L. DiCarlo, J. M. Chow, J. M. Gambetta, L. S. Bishop, B. R. Johnson, D. I. Schuster, J. Majer, A. Blais, L. Frunzio, S. M. Girvin, and R. J. Schoelkopf, Demonstration of two-qubit algorithms with a superconducting quantum processor, *Nature* **460**, 240 (2009).
- [6] A. K. Feofanov, V. A. Oboznov, V. V. Bol’ginov, J. Lisenfeld, S. Poletto, V. V. Ryazanov, A. N. Rossolenko, M. Khabipov, D. Balashov, A. B. Zorin, P. N. Dmitriev, V. P. Koshelets, and A. V. Ustinov, Implementation of superconductor/ferromagnet/superconductor π -shifters in superconducting digital and quantum circuits, *Nature Physics* **6**, 593 (2010).
- [7] W. D. Oliver and P. B. Welander, Materials in superconducting quantum bits, *MRS Bulletin* **38**, 816 (2013).
- [8] K.-H. Lee, S. Chakram, S. E. Kim, F. Mujid, A. Ray, H. Gao, C. Park, Y. Zhong, D. A. Muller, D. I. Schuster, and J. Park, Two-dimensional material tunnel barrier for Josephson junctions and superconducting qubits, *Nano Letters* **19**, 8287 (2019), pMID: 31661615, <https://doi.org/10.1021/acs.nanolett.9b03886>.
- [9] A. P. M. Place, L. V. H. Rodgers, P. Mundada, B. M. Smitham, M. Fitzpatrick, Z. Leng, A. Premkumar, J. Bryon, A. Vrajitoarea, S. Sussman, G. Cheng, T. Madhavan, H. K. Babla, X. H. Le, Y. Gang, B. Jäck, A. Geynis, N. Yao, R. J. Cava, N. P. de Leon, and A. A. Houck, New material platform for superconducting transmon qubits with coherence times exceeding 0.3 milliseconds, *Nature Communications* **12**, 1779 (2021).
- [10] Y. Chen, C. Neill, P. Roushan, N. Leung, M. Fang, R. Barends, J. Kelly, B. Campbell, Z. Chen, B. Chiaro, A. Dunsworth, E. Jeffrey, A. Megrant, J. Y. Mutus, P. J. J. O’Malley, C. M. Quintana, D. Sank, A. Vainsencher, J. Wenner, T. C. White, M. R. Geller, Cle, A. N., and J. M. Martinis, Qubit architecture with high coherence and fast tunable coupling, *Phys. Rev. Lett.* **113**, 220502 (2014).
- [11] M. Kjaergaard, M. E. Schwartz, J. Braumüller, P. Krantz, J. I.-J. Wang, S. Gustavsson, and W. D. Oliver, Superconducting qubits: Current state of play, *Annual Review of Condensed Matter Physics* **11**, 369 (2020), <https://doi.org/10.1146/annurev-conmatphys-031119-050605>.
- [12] R. McDermott, M. G. Vavilov, B. L. T. Plourde, F. K. Wilhelm, P. J. Liebermann, O. A. Mukhanov, and T. A. Ohki, Quantum-classical interface based on single flux quantum digital logic, *Quantum Science and Technology* **3**, 024004 (2018).
- [13] O. Mukhanov, A. Kirichenko, C. Howington, J. Walter, M. Hutchings, I. Vernik, D. Yohannes, K. Dodge, A. Ballard, B. L. T. Plourde, A. Opremcak, C.-H. Liu, and R. McDermott, Scalable quantum computing infrastructure based on superconducting electronics, in *2019 IEEE International Electron Devices Meeting (IEDM)* (2019) pp. 31.2.1–31.2.4.
- [14] J. Koch, T. M. Yu, J. Gambetta, A. A. Houck, D. I. Schuster, J. Majer, A. Blais, M. H. Devoret, S. M. Girvin, and R. J. Schoelkopf, Charge-insensitive qubit design derived from the Cooper pair box, *Phys. Rev. A* **76**, 042319 (2007).
- [15] C. Barthel, D. J. Reilly, C. M. Marcus, M. P. Hanson, and A. C. Gossard, Rapid single-shot measurement of a singlet-triplet qubit, *Phys. Rev. Lett.* **103**, 160503 (2009).
- [16] T. W. Larsen, K. D. Petersson, F. Kuemmeth, T. S. Jespersen, P. Krogstrup, J. Nygård, and C. M. Marcus, Semiconductor-nanowire-based superconducting qubit, *Phys. Rev. Lett.* **115**, 127001 (2015).
- [17] G. de Lange, B. van Heck, A. Bruno, D. J. van Woerkom, A. Geresdi, S. R. Plissard, E. P. A. M. Bakkers, A. R. Akhmerov, and L. DiCarlo, Realization of microwave quantum circuits using hybrid superconducting-semiconducting nanowire Josephson elements, *Phys. Rev. Lett.* **115**, 127002 (2015).
- [18] J. Wiedenmann, E. Bocquillon, R. S. Deacon, S. Hartinger, O. Herrmann, T. M. Klapwijk, L. Maier, C. Ames, C. Brüne, C. Gould, A. Oiwa, K. Ishibashi, S. Tarucha, H. Buhmann, and L. W. Molenkamp, 4π -periodic Josephson supercurrent in HgTe-based topological Josephson junctions, *Nature Communications* **7**, 10303 (2016).
- [19] J. Manousakis, A. Altland, D. Bagrets, R. Egger, and

- Y. Ando, Majorana qubits in a topological insulator nanoribbon architecture, *Phys. Rev. B* **95**, 165424 (2017).
- [20] Ö. Gül, H. Zhang, J. D. S. Bommer, M. W. A. de Moor, D. Car, S. R. Plissard, E. P. A. M. Bakkers, A. Geresdi, K. Watanabe, T. Taniguchi, and L. P. Kouwenhoven, Ballistic Majorana nanowire devices, *Nature Nanotechnology* **13**, 192 (2018).
- [21] J. G. Kroll, W. Uilhoorn, K. L. van der Enden, D. de Jong, K. Watanabe, T. Taniguchi, S. Goswami, M. C. Cassidy, and L. P. Kouwenhoven, Magnetic field compatible circuit quantum electrodynamics with graphene Josephson junctions, *Nature Communications* **9**, 4615 (2018).
- [22] L. Casparis, M. R. Connolly, M. Kjaergaard, N. J. Pearson, A. Kringhøj, T. W. Larsen, F. Kueemeth, T. Wang, C. Thomas, S. Gronin, G. C. Gardner, M. J. Manfra, C. M. Marcus, and K. D. Petersson, Superconducting gatemon qubit based on a proximitized two-dimensional electron gas, *Nature Nanotechnology* **13**, 915 (2018).
- [23] G. Kunakova, A. P. Surendran, D. Montemurro, M. Salvato, D. Golubev, J. Andzane, D. Erts, T. Bauch, and F. Lombardi, Topological insulator nanoribbon Josephson junctions: Evidence for size effects in transport properties, *Journal of Applied Physics* **128**, 194304 (2020), <https://doi.org/10.1063/5.0022126>.
- [24] A. I. Buzdin, Proximity effects in superconductor-ferromagnet heterostructures, *Rev. Mod. Phys.* **77**, 935 (2005).
- [25] M. Minutillo, R. Capecelatro, and P. Lucignano, Realization of $0-\pi$ states in superconductor/ferromagnetic insulator/superconductor Josephson junctions: The role of spin-orbit interaction and lattice impurities, *Phys. Rev. B* **104**, 184504 (2021).
- [26] S. Kawabata, S. Kashiwaya, Y. Asano, Y. Tanaka, and A. A. Golubov, Macroscopic quantum dynamics of π junctions with ferromagnetic insulators, *Phys. Rev. B* **74**, 180502 (2006).
- [27] M. Eschrig and T. Löfwander, Triplet supercurrents in clean and disordered half-metallic ferromagnets, *Nature Physics* **4**, 138 (2008).
- [28] C. Cirillo, V. Pagliarulo, H. Myoren, C. Bonavolontà, L. Parlato, G. P. Pepe, and C. Attanasio, Quasiparticle energy relaxation times in NbN/CuNi nanostripes from critical velocity measurements, *Phys. Rev. B* **84**, 054536 (2011).
- [29] M. G. Blamire and J. W. A. Robinson, The interface between superconductivity and magnetism: understanding and device prospects, *Journal of Physics: Condensed Matter* **26**, 453201 (2014).
- [30] S. M. Dahir, A. F. Volkov, and I. M. Eremin, Phase-dependent spin polarization of Cooper pairs in magnetic Josephson junctions, *Phys. Rev. B* **100**, 134513 (2019).
- [31] K. Serniak, M. Hays, G. de Lange, S. Diamond, S. Shankar, L. D. Burkhardt, L. Frunzio, M. Houzet, and M. H. Devoret, Hot nonequilibrium quasiparticles in transmon qubits, *Phys. Rev. Lett.* **121**, 157701 (2018).
- [32] A. Bilmes, A. Megrant, P. Klimov, G. Weiss, J. M. Martinis, A. V. Ustinov, and J. Lisenfeld, Resolving the positions of defects in superconducting quantum bits, *Scientific Reports* **10**, 3090 (2020).
- [33] M. Weides, M. Kemmler, E. Goldobin, D. Koelle, R. Kleiner, H. Kohlstedt, and A. Buzdin, High quality ferromagnetic 0 and π Josephson tunnel junctions, *Applied Physics Letters* **89**, 122511 (2006), <https://doi.org/10.1063/1.2356104>.
- [34] T. Larkin, V. V. Bol'ginov, V. S. Stolyarov, V. V. Ryazanov, I. V. Vernik, S. K. Tolpygo, and O. A. Mukhanov, Ferromagnetic Josephson switching device with high characteristic voltage, *Applied Physics Letters* **100**, 222601 (2012).
- [35] I. V. Vernik, V. V. Bol'ginov, S. V. Bakurskiy, A. A. Golubov, M. Y. Kupriyanov, V. V. Ryazanov, and O. A. Mukhanov, Magnetic Josephson Junctions with superconducting interlayer for cryogenic memory, *IEEE Transactions on Applied Superconductivity* **23**, 1701208 (2013).
- [36] R. Caruso, D. Massarotti, V. V., A. Ben-Hamida, N. Karelina, A. Miano, I. Vernik, F. Tafuri, V. Ryazanov, O. Mukhanov, and G. P. Pepe, RF assisted switching in magnetic Josephson junctions, *Journal of Applied Physics* **123**, 133901 (2018).
- [37] L. Parlato, R. Caruso, A. Vettoliere, R. Satariano, H. G. Ahmad, A. Miano, D. Montemurro, D. Salvoni, G. Ausanio, F. Tafuri, G. P. Pepe, D. Massarotti, and C. Granata, Characterization of scalable Josephson memory element containing a strong ferromagnet, *Journal of Applied Physics* **127**, 193901 (2020), <https://doi.org/10.1063/5.0004554>.
- [38] L. N. Karelina, R. A. Hovhannisyanyan, I. A. Golovchanskiy, V. I. Chichkov, A. Ben Hamida, V. S. Stolyarov, L. S. Uspenskaya, S. A. Erkenov, V. V. Bolginov, and V. V. Ryazanov, Scalable memory elements based on rectangular SISFS junctions, *Journal of Applied Physics* **130**, 173901 (2021), <https://doi.org/10.1063/5.0063274>.
- [39] K. Senapati, M. G. Blamire, and Z. H. Barber, Spin-filter Josephson junctions, *Nature Materials* **10**, 849 (2011).
- [40] A. P., Z. Barber, J. Robinson, and M. Blamire, Pure second harmonic current-phase relation in spin-filter Josephson junctions, *Nature Communications* **5**, 3340 (2014).
- [41] D. Massarotti, A. Pal, G. Rotoli, L. Longobardi, M. G. Blamire, and F. Tafuri, Macroscopic quantum tunnelling in spin filter ferromagnetic Josephson junctions, *Nature Communications* **6**, 7376 (2015).
- [42] R. Caruso, D. Massarotti, G. Campagnano, A. Pal, H. G. Ahmad, P. Lucignano, M. Eschrig, M. G. Blamire, and F. Tafuri, Tuning of magnetic activity in spin-filter Josephson junctions towards spin-triplet transport, *Phys. Rev. Lett.* **122**, 047002 (2019).
- [43] H. Ahmad, R. Caruso, A. Pal, G. Rotoli, G. Pepe, M. Blamire, F. Tafuri, and D. Massarotti, Electrodynamics of highly spin-polarized tunnel Josephson junctions, *Phys. Rev. Applied* **13**, 014017 (2020).
- [44] H. G. Ahmad, M. Minutillo, R. Capecelatro, A. Pal, R. Caruso, G. Passarelli, M. G. Blamire, F. Tafuri, P. Lucignano, and D. Massarotti, Coexistence and tuning of spin-singlet and triplet transport in spin-filter Josephson junctions, *Communications Physics* **5**, 2 (2022).
- [45] J. P. Cascales, Y. Takamura, G. M. Stephen, D. Heiman, F. S. Bergeret, and J. S. Moodera, Switchable Josephson junction based on interfacial exchange field, *Applied Physics Letters* **114**, 022601 (2019), <https://doi.org/10.1063/1.5050382>.
- [46] R. Satariano, L. Parlato, A. Vettoliere, R. Caruso, H. G. Ahmad, A. Miano, L. Di Palma, D. Salvoni, D. Montemurro, C. Granata, G. Lamura, F. Tafuri, G. P. Pepe, D. Massarotti, and G. Ausanio, Inverse magnetic hysteresis of the Josephson supercurrent: Study of the magnetic

- properties of thin niobium/permalloy ($\text{Fe}_{20}\text{Ni}_{80}$) interfaces, *Phys. Rev. B* **103**, 224521 (2021).
- [47] A. Barone and G. Paternò, *Physics and Application of the Josephson Effect* (John Wiley and Sons, 1982).
- [48] F. Tafuri, J. R. Kirtley, F. Lombardi, and F. M. Granozio, Intrinsic and extrinsic d-wave effects in $\text{YBa}_2\text{Cu}_3\text{O}_{7-\delta}$ grain boundary Josephson junctions: Implications for π circuitry, *Phys. Rev. B* **67**, 174516 (2003).
- [49] M. G. Blamire, C. B. Smiet, N. Banerjee, and J. W. A. Robinson, Field modulation of the critical current in magnetic Josephson junctions, *Superconductor Science and Technology* **26**, 055017 (2013).
- [50] M. G. Blamire, A. Pal, Z. H. Barber, and K. S., *Spin filter superconducting tunnel junctions* (2012).
- [51] A. Wallraff, D. I. Schuster, A. Blais, L. Frunzio, R.-S. Huang, J. Majer, S. Kumar, S. M. Girvin, and R. J. Schoelkopf, Strong coupling of a single photon to a superconducting qubit using circuit quantum electrodynamics, *Nature* **431**, 162 (2004).
- [52] J. Majer, J. M. Chow, J. M. Gambetta, J. Koch, B. R. Johnson, J. A. Schreier, L. Frunzio, D. I. Schuster, A. A. Houck, A. Wallraff, A. Blais, M. H. Devoret, S. M. Girvin, and R. J. Schoelkopf, Coupling superconducting qubits via a cavity bus, *Nature* **449**, 443 (2007).
- [53] M. D. Hutchings, J. B. Hertzberg, Y. Liu, N. T. Bronn, G. A. Keefe, M. Brink, J. M. Chow, and B. L. T. Plourde, Tunable superconducting qubits with flux-independent coherence, *Phys. Rev. Applied* **8**, 044003 (2017).
- [54] W. Dietrich, W. E. Proebster, and P. Wolf, Nanosecond switching in thin magnetic films, *IBM Journal of Research and Development* **44**, 167 (2000).
- [55] Y. Sung, L. Ding, J. Braumüller, A. Vepsäläinen, B. Kannan, M. Kjaergaard, A. Greene, G. O. Samach, C. McNally, D. Kim, A. Melville, B. M. Niedzielski, M. E. Schwartz, J. L. Yoder, T. P. Orlando, S. Gustavsson, and W. D. Oliver, Realization of high-fidelity CZ and ZZ-free iSWAP gates with a tunable coupler, *Phys. Rev. X* **11**, 021058 (2021).
- [56] O. A. Mukhanov, Energy-efficient single flux quantum technology, *IEEE Transactions on Applied Superconductivity* **21**, 760 (2011).
- [57] S. V. Bakurskiy, N. V. Klenov, I. I. Soloviev, V. V. Bol'ginov, V. V. Ryazanov, I. V. Vernik, O. A. Mukhanov, M. Y. Kupriyanov, and A. A. Golubov, Theoretical model of superconducting spintronic SISFS devices, *Applied Physics Letters* **102**, 192603 (2013), <https://doi.org/10.1063/1.4805032>.
- [58] S. Probst, F. B. Song, P. A. Bushev, A. V. Ustinov, and M. Weides, Efficient and robust analysis of complex scattering data under noise in microwave resonators, *Review of Scientific Instruments* **86**, 024706 (2015), <https://doi.org/10.1063/1.4907935>.
- [59] D. M. Pozar, *Microwave engineering* (John Wiley & sons, 2011).
- [60] A. Blais, R.-S. Huang, A. Wallraff, S. M. Girvin, and R. J. Schoelkopf, Cavity quantum electrodynamics for superconducting electrical circuits: An architecture for quantum computation, *Phys. Rev. A* **69**, 062320 (2004).
- [61] C. Rigetti, J. M. Gambetta, S. Poletto, B. L. T. Plourde, J. M. Chow, A. D. Córcoles, J. A. Smolin, S. T. Merkel, J. R. Rozen, G. A. Keefe, M. B. Rothwell, M. B. Ketchen, and M. Steffen, Superconducting qubit in a waveguide cavity with a coherence time approaching 0.1 ms, *Phys. Rev. B* **86**, 100506 (2012).
- [62] Y. Nakamura, H. Terai, K. Inomata, T. Yamamoto, W. Qiu, and Z. Wang, Superconducting qubits consisting of epitaxially grown NbN/AlN/NbN Josephson junctions, *Applied Physics Letters* **99**, 212502 (2011), <https://doi.org/10.1063/1.3663539>.
- [63] S. Kim, H. Terai, T. Yamashita, W. Qiu, T. Fuse, F. Yoshihara, S. Ashhab, K. Inomata, and K. Semba, Enhanced-coherence all-nitride superconducting qubit epitaxially grown on Si substrate (2021), [arXiv:2103.07711](https://arxiv.org/abs/2103.07711) [quant-ph].
- [64] B. D. Cullity and C. D. Graham, *Introduction to magnetic materials* (John Wiley & Sons, 2011).
- [65] V. V. Bol'ginov, O. A. Tikhomirov, and L. S. Uspenskaya, Two-component magnetization in $\text{Pd}_{99}\text{Fe}_{01}$ thin films, *JETP Letters* **105**, 169 (2017).
- [66] P. Krantz, A. Bengtsson, M. Simoen, S. Gustavsson, V. Shumeiko, W. D. Oliver, C. M. Wilson, P. Delsing, and J. Bylander, Single-shot read-out of a superconducting qubit using a Josephson parametric oscillator, *Nature Communications* **7**, 11417 (2016).
- [67] A. Khanna and Y. Garault, Determination of loaded, unloaded, and external quality factors of a dielectric resonator coupled to a microstrip line, *IEEE Transactions on Microwave Theory and Techniques* **31**, 261 (1983).
- [68] A. Palacios-Laloy, F. Nguyen, F. Mallet, P. Bertet, D. Vion, and D. Esteve, Tunable resonators for quantum circuits, *Journal of Low Temperature Physics* **151**, 1034 (2008).
- [69] M. Partanen, K. Y. Tan, S. Masuda, J. Govenius, R. E. Lake, M. Jenei, L. Grönberg, J. Hassel, S. Simbierowicz, V. Vesterinen, J. Tuorila, T. Ala-Nissila, and M. Möttönen, Flux-tunable heat sink for quantum electric circuits, *Scientific Reports* **8**, 6325 (2018).
- [70] V. V. Ryazanov, V. V. Bol'ginov, D. S. Sobanin, I. V. Vernik, S. K. Tolpygo, A. M. Kadin, and O. A. Mukhanov, Magnetic Josephson junction technology for digital and memory applications, *Physics Procedia* **36**, 35 (2012).
- [71] R. Caruso, D. Massarotti, A. Miano, V. V. Bolginov, A. B. Hamida, L. N. Karelina, G. Campagnano, I. V. Vernik, F. Tafuri, V. V. Ryazanov, O. A. Mukhanov, and G. P. Pepe, Properties of ferromagnetic Josephson Junctions for memory applications, *IEEE Transactions on Applied Superconductivity* **28**, 1 (2018).
- [72] U. Vool and M. Devoret, Introduction to quantum electromagnetic circuits, *International Journal of Circuit Theory and Applications* **45**, 897 (2017), <https://onlinelibrary.wiley.com/doi/pdf/10.1002/cta.2359>.
- [73] W. C. Smith, *Design of protected superconducting qubits*, Ph.D. thesis, Yale University (2019).
- [74] E. A. Sete, J. M. Gambetta, and A. N. Korotkov, Purcell effect with microwave drive: Suppression of qubit relaxation rate, *Phys. Rev. B* **89**, 104516 (2014).
- [75] G. Ithier, E. Collin, P. Joyez, P. J. Meeson, D. Vion, D. Esteve, F. Chiarello, A. Shnirman, Y. Makhlin, J. Schrieffer, and G. Schön, Decoherence in a superconducting quantum bit circuit, *Phys. Rev. B* **72**, 134519 (2005).
- [76] A. Bruno, B. Cinzia, B. Giorgio, and M. Arianna, Domain wall dynamics and Barkhausen effect in metallic ferromagnetic materials. II. experiments, *Journal of Applied Physics* **68**, 2908 (1990), <https://doi.org/10.1063/1.346424>.
- [77] S. Yamaura, Y. Furuya, and T. Watanabe, The effect

- of grain boundary microstructure on Barkhausen noise in ferromagnetic materials, *Acta Materialia* **49**, 3019 (2001).
- [78] R. Vardimon, M. Matt, P. Nielaba, J. C. Cuevas, and O. Tal, Orbital origin of the electrical conduction in ferromagnetic atomic-size contacts: Insights from shot noise measurements and theoretical simulations, *Phys. Rev. B* **93**, 085439 (2016).
- [79] M. Gijs, J. Giesbers, P. Beliën, J. van Est, J. Briaire, and L. Vandamme, $1/f$ noise in magnetic Ni80Fe20 single layers and Ni80Fe20/Cu multilayers, *J. Magn. Magn. Mater.* **165**, 360 (1997).
- [80] M. Ocio, H. Bouchiat, and P. Monod, Observation of $1/f$ magnetic fluctuations in spin glasses, *J. Magn. Magn. Mater.* **54-57**, 11 (1986).
- [81] A. Balk, F. Li, I. Gilbert, J. Unguris, N. Sinitsyn, and S. Crooker, Broadband spectroscopy of thermodynamic magnetization fluctuations through a ferromagnetic spin-reorientation transition, *Phys. Rev. X* **8**, 031078 (2018).
- [82] S. M. Anton, C. Müller, J. S. Birenbaum, S. R. O’Kelley, A. D. Fefferman, D. S. Golubev, G. C. Hilton, H.-M. Cho, K. D. Irwin, F. C. Wellstood, G. Schön, A. Shnirman, and J. Clarke, Pure dephasing in flux qubits due to flux noise with spectral density scaling as $1/f\alpha$, *Physical Review B* **85**, 10.1103/physrevb.85.224505 (2012).
- [83] S. Kempf, A. Ferring, and C. Enss, Towards noise engineering: Recent insights in low-frequency excess flux noise of superconducting quantum devices, *Applied Physics Letters* **109**, 162601 (2016).
- [84] F. Yan, S. Gustavsson, A. Kamal, J. Birenbaum, A. P. Sears, D. Hover, T. J. Gudmundsen, D. Rosenberg, G. Samach, S. Weber, J. L. Yoder, T. P. Orlando, J. Clarke, A. J. Kerman, and W. D. Oliver, The flux qubit revisited to enhance coherence and reproducibility, *Nature Communications* **7**, 12964 (2016).
- [85] C. M. Quintana, Y. Chen, D. Sank, A. G. Petukhov, T. C. White, D. Kafri, B. Chiaro, A. Megrant, R. Barends, B. Campbell, Z. Chen, A. Dunsworth, A. G. Fowler, R. Graff, E. Jeffrey, J. Kelly, E. Lucero, J. Y. Mutus, M. Neeley, C. Neill, P. J. J. O’Malley, P. Roushan, A. Shabani, V. N. Smelyanskiy, A. Vainsencher, J. Wenner, H. Neven, and J. M. Martinis, Observation of classical-quantum crossover of $1/f$ flux noise and its paramagnetic temperature dependence, *Phys. Rev. Lett.* **118**, 057702 (2017).
- [86] G. Duffing, *Erzwungene Schwingungen bei veränderlicher Eigenfrequenz und ihre technische Bedeutung*, 41-42 (Vieweg, 1918).
- [87] G. Wild, C. Probst, A. Marx, and R. Gross, Josephson coupling and Fiske dynamics in ferromagnetic tunnel junctions, *The European Physical Journal B* **78**, 509 (2010).